



HAL
open science

Solute effects on dynamics and deformation of emulsion droplets during freezing

Sidhanth Tyagi, Cécile Monteux, Sylvain Deville

► **To cite this version:**

Sidhanth Tyagi, Cécile Monteux, Sylvain Deville. Solute effects on dynamics and deformation of emulsion droplets during freezing. *Soft Matter*, 2022, 10.1039/D2SM00226D . hal-03274394v1

HAL Id: hal-03274394

<https://hal.science/hal-03274394v1>

Submitted on 8 Oct 2021 (v1), last revised 7 Jul 2022 (v3)

HAL is a multi-disciplinary open access archive for the deposit and dissemination of scientific research documents, whether they are published or not. The documents may come from teaching and research institutions in France or abroad, or from public or private research centers.

L'archive ouverte pluridisciplinaire **HAL**, est destinée au dépôt et à la diffusion de documents scientifiques de niveau recherche, publiés ou non, émanant des établissements d'enseignement et de recherche français ou étrangers, des laboratoires publics ou privés.

1 Solute effects on dynamics and deformation of
2 emulsion droplets during freezing

3 Sidhanth Tyagi^{1,2}, Cécile Monteux^{2,3}, and Sylvain Deville⁴

4 ¹*Laboratoire de Synthèse et Fonctionnalisation des Céramiques, UMR 3080*
5 *CNRS/Saint-Gobain CREE, Saint-Gobain Research Provence, Cavaillon, France.*

6 ²*Sciences et Ingénierie de la Matière Molle, ESPCI Paris, PSL Research University,*
7 *CNRS, Sorbonne Universités, UPMC Univ Paris 06, Paris, France.*

8 ³*Global Station for Soft Matter, Global Institution for Collaborative Research and*
9 *Education, Hokkaido University, Sapporo, Japan.*

10 ⁴*Université de Lyon, Université Claude Bernard Lyon1, CNRS, Institut Lumière*
11 *Matière, 69622 Villeurbanne, France.*

12 June 25, 2021

13 **Abstract**

14 Soft or rigid particles, suspended in a liquid melt, interact with an advancing
15 solidification front in various industrial and natural processes, such as fabrica-
16 tion of particle-reinforced-composites, growth of crystals, cryopreservation, frost
17 heave, and growth of sea ice. The particle dynamics relative to the front de-
18 termine the microstructure as well as the functional properties of the solidified
19 material. The previous studies have extensively investigated the interaction of
20 foreign objects with a moving solid-liquid interface in pure melts while in most
21 real-life systems, solutes or surface active impurities are almost always present.
22 Here we study experimentally the interaction of spherical oil droplets with a

23 moving planar ice-water interface, while systematically increasing the surfac-
24 tant concentration in the bulk liquid, using *in situ* cryo-confocal microscopy.
25 We demonstrate that a small amount of surfactant in the bulk liquid can insti-
26 gate long-range droplet repulsion, extending over a length scale of 40 to 100 μm ,
27 in contrast to the short-range predicted previously ($< 1 \mu m$). We report on the
28 droplet deformation, while they are in contact with the ice-water interface, as a
29 function of the bulk surfactant concentration, the droplet size, and the crystal
30 growth rate. We also depict the dynamic evolution of solute-enriched premelted
31 films ($\approx 5 \mu m$). Our results demonstrate how an increasing concentration of
32 surfactant in the bulk and its subsequent segregation during solidification can
33 dramatically alter the solidification microstructures. We anticipate that our
34 experimental study can serve for the development of theoretical models incor-
35 porating solute effects.

36 *Keywords: solidification, solute, droplets, deformation, dynamics*

37 1 Introduction

38 The interaction of particles with an approaching solid-liquid interface is of spe-
39 cial relevance in nature, like frost heave, glacial motion [1], and in engineering
40 sciences, such as food freeze-thaw stability [2], cryopreservation [3, 4], metal-
41 lurgy [5], and crystal growth [6]. This dynamic problem consists of particles,
42 soft or hard, dispersed in a liquid melt interacting with a solid-liquid interface.
43 The objects can be biological cells in cryopreservation [3, 4], colloids in freeze-
44 casting [7], droplets in food preservation [8], gas bubbles in growth of single
45 crystals [6, 9] and metallurgy [5], or reinforcing particles in material-matrix-
46 composites [10]. The outcome of the particle-interface confrontation determines
47 the solidified microstructure and hence, the functional properties of the solidi-
48 fied material. Thus, it is essential to understand the underlying mechanisms of
49 solidification (or freezing) to forge the required material microstructure. The
50 particle can interact with an advancing solidification interface with diverse out-
51 comes; it can be engulfed instantaneously upon contact, pushed ahead in the
52 remaining liquid by the interface indefinitely, or it may undergo engulfment after
53 being pushed over a certain distance [11].

54 The dynamics of interaction and spatial distribution of particles are essential
55 features in several material fabrication routes. In particle-reinforced-composites,
56 an instantaneous engulfment in solid phase is desired as it facilitates a homo-
57 geneous distribution of the suspended objects [10]. In metallurgy and crystal
58 growth, a continuous repulsion of the impurities by the interface is required to
59 obtain impurity-free-solids [5]. In freeze-casting, a segregation of the colloidal
60 particles by the growing solid enables a porous material structure [7]. The
61 shape of the particle (deformed or undeformed) becomes an equally important
62 processing criterion in applications where soft deformable objects (droplets or
63 bubbles) encounter a moving solid-liquid interface. In cryobiology, utmost care
64 should be taken to avoid physical injury inflicted to the cells from the growing
65 ice crystals [12]. In food preservation, freezing is conducted to conserve the

66 size, shape, and distribution of the dispersed droplets, thereby preserving the
67 original taste and appearance [8]. Thus, numerous interaction scenarios, still
68 poorly understood, can exist during solidification.

69 The role and concentration of solute in the solidifying liquid is often signifi-
70 cant and a dominating factor in determining, amongst others, the shape of the
71 solid-liquid interface in the vicinity of the suspended particles [13–15]. Solutes,
72 render the interfacial curvature concave, thereby promoting engulfment of ob-
73 jects at growth rates lower than those predicted for planar curvatures [16, 17].
74 The solutes can be either desired, like additives (e.g. cryoprotectant used in
75 preservation of biological cells), or be present as an undesired impurity, such as
76 dissolved gases (H_2) in liquid metals or surface active impurities. The segrega-
77 tion of solutes at the interface is instigated by their relatively low solubility in
78 the solid phase and enhanced further by the approaching objects obstructing
79 their diffusion field [13]. This local solute enrichment is of particular impor-
80 tance in understanding the nucleation and growth of macroporosity in solid-
81 ifying melts [14], studying the constitutional supercooling with formation of
82 premelted films [18, 19], and in determining the osmotic stresses acting on a
83 freezing biological cell [4, 12] to give a few examples. Moreover, the morphology
84 of a solid-liquid interface (planar, columnar, or dendritic), determined by the
85 magnitude of solute concentration gradient build-up ahead of the growing solid,
86 plays a major role on the final microstructure [13, 20].

87 The study of solidification mechanisms such as the particle dynamics, shape
88 evolution, and the local solute concentration are complex and require *in situ* in-
89 vestigations. The major problem associated with studying solidification *in situ*
90 arises from the need of high space and temporal resolution in conjunction with
91 elevated temperatures especially for metals. For the object dynamics, past stud-
92 ies have formulated a plethora of analytical and numerical models expressing
93 the outcome (engulfment or rejection) of objects interacting at close distances
94 ($< 10\text{ nm}$) with the solid-liquid interface [16, 21–24]. The models vary in the
95 mathematical formulation of the features taken into account (e.g. the inclusion

96 of object-melt thermal conductivity mismatch, solute effects etc. . .), while using
97 a similar approach (balance of repulsive and attractive forces between the object
98 and front) to describe the interaction [11]. The study of particle deformation
99 has been of particular interest in the prediction of pore shape evolution during
100 directional solidification of crystals to avoid or control porosity defects. Much
101 of the progress in this domain has been achieved through numerical simulations
102 and post-solidification analysis [25, 26]. *In situ* experimental evidence of solidi-
103 fication dynamics (repulsion or engulfment) and shape modification have been
104 facilitated using transparent analogs (e.g. succinonitrile-acetone) with optical
105 microscopes at ambient temperatures [20, 27] and X-ray transmission microscope
106 at elevated temperatures [14, 28]. However, the volume investigated along with
107 the temporal resolution is limited, while the local solute segregation cannot be
108 visualized. Hence, the tracking of microstructures where objects interact with
109 a solid-liquid interface in the presence of solute effects remains challenging.

110 In this study, we analyse the interaction of spherical oil droplets with an ad-
111 vancing ice-water interface using *in situ* cryo-confocal microscopy. Our custom
112 solidification setup enables a small temporal resolution (1.7 s) and high spatial
113 resolution (1024×1024 pixels) with laser-induced fluorescence to distinguish the
114 accumulation of a fluorescent water-soluble dye rejected by the ice. We prepare
115 oil-in-water emulsions using microfluidics stabilized with a varying amount of
116 surfactant Tween 80 in the aqueous phase. We further characterise and report
117 on the *in situ* droplet dynamics, droplet deformation, and the role of surfactant
118 on the droplet behaviour.

119 We investigate the impact of an increasing surfctant concentration on the
120 mechanisms involved at three different stages: droplets in water (water) far
121 from the solidification front, droplets in contact with an approaching solid-
122 liquid interface, and droplets captured in the growing ice. For the droplet-front
123 interaction dynamics, we depict distinct behaviours such as instantaneous en-
124 gulfment and repulsion-engulfment transition. While confronting a solid-liquid
125 interface, the droplet shape evolution depends on the imposed growth rate and

126 the surfactant concentration. Furthermore, we show the impact of surfactant
127 on the evolution of premelted films surrounding the oil droplets in ice. Fi-
128 nally, we depict that the three interaction stages are crucial in determining the
129 droplet spatial distribution and shape evolution, and hence, the solidification
130 microstructure.

131 **2 Methods**

132 **2.1 Materials**

133 We purchased the oil (propyl benzoate), surfactant (Tween 80), oil fluorophore
134 (Difluoro2-[1-(3,5-dimethyl-2H-pyrrol-2-ylidene-N)ethyl]-3,5-dimethyl-1H-pyrro-
135 lato-Nboron), and aqueous fluorophore (Sulforhodamine B) from Sigma-Aldrich.
136 The fluorophores are referred to as BODIPY (incorporated in oil) and SRhB
137 (incorporated in water) in the study. We cycled the deionized water through
138 $0.45 \mu\text{m}$ Nylon membrane filters (VWR International) to remove traces of im-
139 purities and ensure purity of the emulsions prepared. The solidification ex-
140 periments were conducted to study the interaction of dispersed phase with the
141 ice-water interface. Hence, we prepared oil-in-water emulsions to ensure the
142 dispersed phase remained liquid, while the continuous phase underwent solidi-
143 fication. Thus, we chose propyl benzoate owing to its low melting temperature
144 ($T_m = -51.6^\circ \text{C}$), low solubility in water ($0.035 \text{ g}/100 \text{ g}$), and similar density
145 to water ($\rho_{oil} = 1.023 \text{ g} \cdot \text{cm}^{-3}$).

146 **2.2 Sample Preparation**

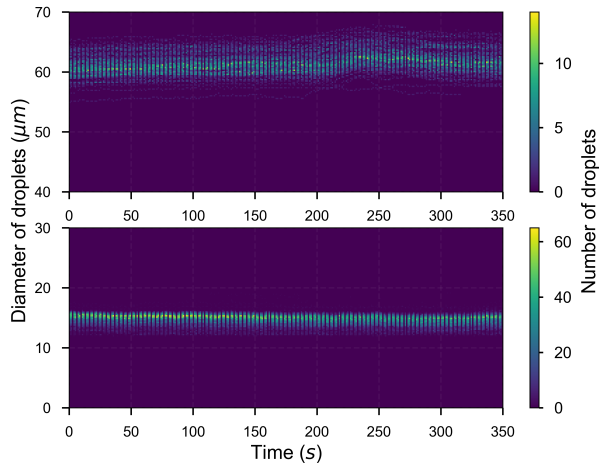


Figure 1: **Diameter of monodisperse droplets with radii (R_1, R_2) of $7.2 \pm 0.4 \mu m$ and $30.9 \pm 1.2 \mu m$ respectively, generated using microfluidics.** The size of droplets remained stable during the experimental time-scale, which varied from 15 min to 4 h. © (2020) S. Tyagi *et al.* (10.6084/m9.figshare.14815083) CC BY 4.0 license <https://creativecommons.org/licenses/by/4.0/>.

147 We prepared the oil-in-water emulsions using a microfluidic setup, as explained
 148 in our previous study [15]. The monodisperse droplets have radii (R_1, R_2) of
 149 either $7.2 \pm 0.4 \mu m$ or $30.9 \pm 1.2 \mu m$, as shown in Fig.1. The oil phase consisted
 150 of propyl benzoate with $10^{-4} M$ BODIPY to obtain clear imaging of dispersed
 151 droplets at 1% laser power. For the aqueous phase, we used $10^{-5} M$ SRhB
 152 solution, as self-quenching was reported at concentrations above $2 \times 10^{-4} M$ [29].
 153 We added Tween 80 ($HLB = 15$ [30]), a non-ionic surfactant, to the aqueous
 154 phase to stabilise the oil droplets. The surfactant Tween 80 ($cmc = 13 - 15 mg \cdot$
 155 l^{-1} [31]) also acts as a solute and hence colligatively depresses the freezing point
 156 of solutions, when its concentration increases locally [15]. We prepared three
 157 aqueous solutions with 0.01, 0.1, and 1 wt.% Tween 80 to study the impact of
 158 solute concentration on the solidification dynamics and behaviour of oil droplets
 159 dispersed in an aqueous phase. The surfactant is added as wt.% of the aqueous
 160 solution to have an equal concentration in all the solutions prepared.

161 The concentration of surfactants in the bulk solution at which micelles start
 162 forming is known as the *cmc*. Individual surfactant molecules that are in the
 163 system but are not part of a micelle are called monomers [32]. At 1wt.% of
 164 Tween 80 in aqueous solution we are $\approx 600 \times cmc$. All experiments are therefore
 165 performed above the *cmc* and increasing the surfactant concentration results
 166 in an increase of the number of micelles in solution while the concentration
 167 of surfactant monomers remains approximatively equal to the *cmc*. The oil-
 168 in-water emulsion stabilized by the surfactant is represented schematically in
 169 Fig.2. The presence of micelles at the given concentration was confirmed by
 170 dynamic light scattering (DLS) analysis. A typical micelle size of 9 nm with a
 171 corresponding diffusion coefficient of $30 \mu m^2 \cdot s^{-1}$ at 273 K was obtained from
 172 the DLS analysis. The prepared emulsions were filled through capillarity and
 173 solidified in a rectangular Hele-Shaw cell (height = 100 μm and volume = 100 μl).
 174 We fabricated the Hele-Shaw cell using two glass slides (Menzel, $24 \times 60 mm$,
 175 thickness 0.13 – 0.16 mm), and sealed it with nail-polish at one end to prevent
 176 evaporation and leakage.

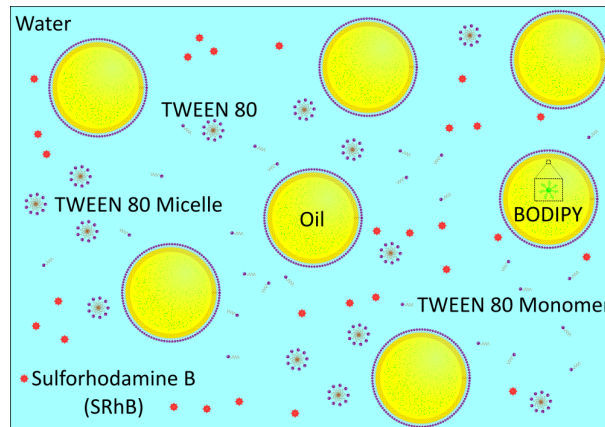


Figure 2: **Schematic depicting a monodisperse oil-in-water emulsion with the surfactant Tween 80 and fluorophore SRhB added to the aqueous phase (not to scale). The oil phase is incorporated with the fluorophore BODIPY.** The surfactant form micelles. © (2020) S. Tyagi *et al.* (10.6084/m9.figshare.14815083) CC BY 4.0 license <https://creativecommons.org/licenses/by/4.0/>.

177 2.3 Imaging & Analysis

178 We used a Leica TCS SP8 confocal laser scanning microscope (Leica Microsys-
 179 temes SAS, Germany) equipped with 488 nm (blue), 552 nm (green) lasers and
 180 two photodetectors (PMT) for image acquisition. The images were captured
 181 for the emission spectra of BODIPY (oil phase) and SRhB (aqueous phase),
 182 using a non-immersive objective (Leica HCX PL APO CS 20 \times) with a working
 183 distance of 590 μm . Ice does not fluoresce and hence, we can simultaneously
 184 detect three phases (oil droplets, unfrozen aqueous phase, and ice) with two
 185 photodetectors. In $2D$, we used the microscope at a scanning speed of 600 Hz,
 186 with 1024×1024 pixels for imaging 775×775 μm , resulting in 1.7 s per frame.
 187 We used Fiji [33] for image thresholding in conjunction with Python [34] for
 188 image and data analysis.

189 2.4 Freezing Stage

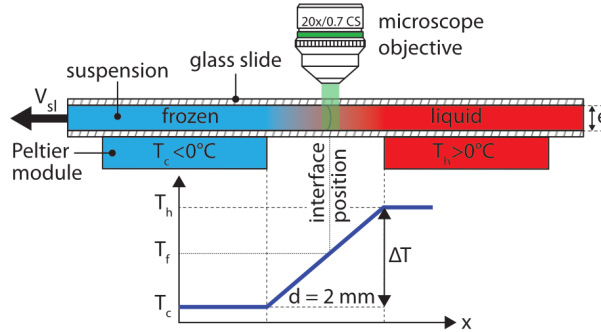


Figure 3: **Cryo-confocal microscope setup to perform *in situ* solidification experiments.** A Hele-Shaw cell containing an oil-in-water emulsion is pulled at a constant velocity (V_{sl}) through a constant linear temperature gradient (G), established by two Peltier elements. In *steady-state*, the solidification interface is at a constant position under the microscope objective. In the sample frame, the interface is moving at a solidification velocity of V_{sl} , imposed by the motor. © (2020) S. Tyagi *et al.* (10.6084/m9.figshare.12046560) CC BY 4.0 license <https://creativecommons.org/licenses/by/4.0/>.

190 We conducted unidirectional solidification experiments, translating the sample
 191 cell at a constant velocity (V_{sl}) along a constant linear temperature gradient (G)

192 of $10^4 \text{ K} \cdot \text{m}^{-1}$, using the cryo-confocal stage described in detail previously [35].
 193 We imposed the temperature with two Peltier modules, and controlled it with
 194 high precision ($< 0.01 \text{ }^\circ\text{C}$) using TEC-1122 Dual Thermo Electric Cooling Tem-
 195 perature Controller from Meerstetter Engineering, Switzerland. The Peltier el-
 196 ements were separated by a distance of 2 mm to establish a linear temperature
 197 gradient along \vec{x} . The *in situ* observation of objects interacting with the solid-
 198 liquid interface was achieved using a confocal microscope mounted vertically
 199 over the gap (2 mm) between the two Peltier modules, as shown in Fig.3. The
 200 solidification interface appears immobile in the frame of observation, however,
 201 in the sample frame, a solidifying front at the velocity V_{sl} is advancing in the
 202 sample (along \vec{x}). We utilised the VT-80 translation stage (Micos Pollux Drive
 203 PI, USA) to impose the rate at the which the sample cell is pulled through the
 204 temperature gradient. The rate of translation was verified to be in agreement
 205 with the measured solidification velocity (V_{sl}), using posterior image analysis
 206 (*error* $< 1 \%$). Thus, we can decouple and control independently the solidifica-
 207 tion velocity (V_{sl}) and the thermal gradient (G) in our system.

208 We performed the solidification experiments in the velocity range of
 209 $1.0 \leq V_{sl} \leq 10.0 \text{ } \mu\text{m} \cdot \text{s}^{-1}$. We wait for $20 - 30 \text{ mins}$ to ensure a *steady-*
 210 *state* diffusion controlled regime before starting the acquisition at a given so-
 211 lidification velocity. The time needed for a steady-state to establish scales as
 212 $2D/V_{sl}^2 \approx 60 \text{ s}$, where D is the solute diffusion coefficient. We do not expect
 213 forced convection in our experiments as they are performed in a closed Hele-
 214 Shaw cell of small thickness ($100 \text{ } \mu\text{m}$) and at low solidification velocity with
 215 a steady linear temperature gradient. The solid-liquid interface is stable over
 216 extended time periods ($\approx 4 - 5 \text{ hours}$) and the interface does not accelerate or
 217 decelerate during the solidification experiments. In addition, we do not observe
 218 a transient unsteady regime and the interface morphology is stable for the given
 219 experimental parameters.

3 Results & Discussions

We performed horizontal solidification experiments by displacing a Hele-Shaw cell, containing an oil-in-water emulsion, in a custom cryo-confocal stage, at a velocity of V_{sl} . A typical $2D$ confocal image of a freezing emulsion with the distinct features observed is shown in Fig.4A. The confocal image enables us to distinguish three phases; oil phase in cyan (fluorophore BODIPY), water in colormap viridis (fluorophore SRhB), and a dark ice phase. As solidification progresses, the growing ice phase rejects the dissolved dye, SRhB, owing to its low solubility and hence appears black, which enables us to visualize the solid-liquid interface. In the frame of the ice-water interface, the interface is stationary and the droplets far from the ice-water interface are translated at a velocity V_{sl} toward the ice-water interface. In the frame of the sample, the interface is advancing through the sample at a velocity of V_{sl} along \vec{x} and eventually encounters droplets which velocity, noted U_r (defined in Fig. S2) is indicated in Fig.4A. We also note the premelted films between two ice surfaces as well as around the oil droplets captured in the ice phase, which are due to the rejection of the dye by the ice and subsequent depression of the freezing point.

A typical time-lapse evolution of an isolated oil droplet interacting with the ice-water interface obtained for an oil-in-water emulsion with $1wt.\%$ Tween 80 in the aqueous phase is shown in Fig.4B. The interaction of oil droplets with the solid-liquid interface can be divided in three different stages, which are described below in three different sections. First, we investigate the solidification mechanisms at play when the oil droplets are far from the advancing interface. We investigate the role of an increasing bulk surfactant concentration and the different solidification parameters (growth rate, droplet size) on the droplet dynamics in water ($t < 44$ s in Fig.4B). Second, we look into the impact of the approaching solid-liquid interface on the droplet shape upon their mutual contact ($44 \leq t \leq 57$ s in Fig.4B). Third, we analyse the droplets captured in ice and report on the evolution of premelted films with the associated ice-water

249 meniscus ($99 \leq t \leq 111$ s in Fig.4B).

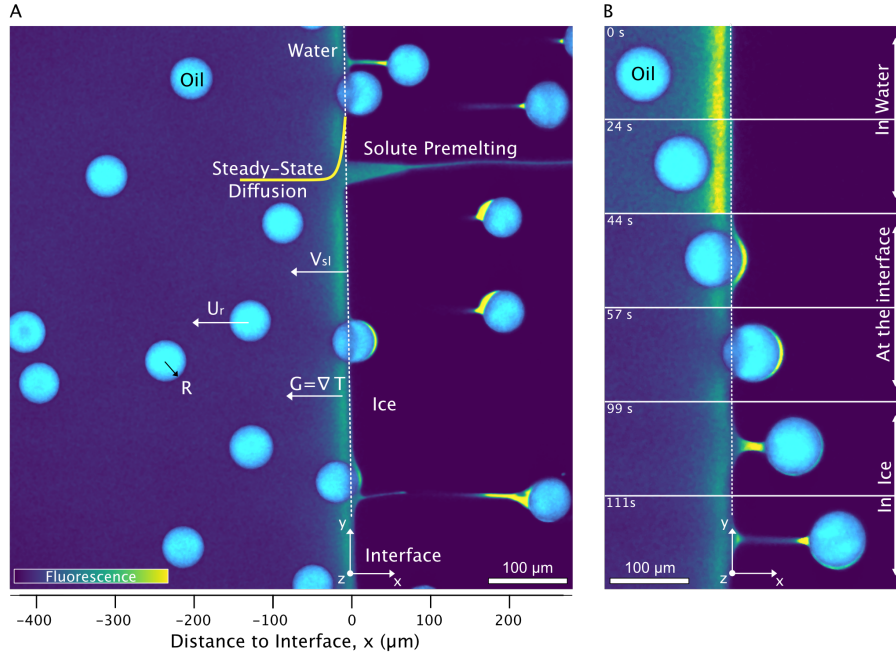


Figure 4: **2D cryo-confocal image of freezing an oil-in-water emulsion in the presence of 1wt.% Tween 80 in the aqueous phase.** (A) Typical features observed for a planar growth at $V_{sl} = 2 \mu\text{m} \cdot \text{s}^{-1}$ (B) Time-lapse evolution of an oil droplet encountering an approaching solid-liquid interface with three distinct regimes of interaction at $V_{sl} = 2 \mu\text{m} \cdot \text{s}^{-1}$. Ice is in black, oil droplets in cyan, and the aqueous phase is in colormap viridis (fluorescence bar). © (2020) S. Tyagi *et al.* (10.6084/m9.figshare.14815083) CC BY 4.0 license <https://creativecommons.org/licenses/by/4.0/>.

250 3.1 Droplets in water

251 We track the trajectories of the oil droplets which enables us to deduce the
 252 isolated droplet velocity U_r in the sample frame (see details in Fig. S1 and
 253 S2). Our Hele-Shaw cell of length 4 cm facilitates an acquisition of 50 – 400
 254 isolated droplet velocities and we deduce the mean droplet velocity as $\bar{U} = \langle U_r \rangle$
 255 (The python script employed can be found in a previous study [19]). A positive
 256 magnitude of \bar{U} implies that the droplets are repelled or pushed by the moving
 257 ice-water interface towards the remaining liquid.

258 In Fig.5, we present the mean droplet velocity, \bar{U} , with the distance to

259 interface for an interface velocity of V_{sl} of $3 \mu m \cdot s^{-1}$. We define the distance to
 260 interface as $0 \mu m$ when the front edge of the droplet comes in contact with the
 261 absolute detected position of the ice-water interface.

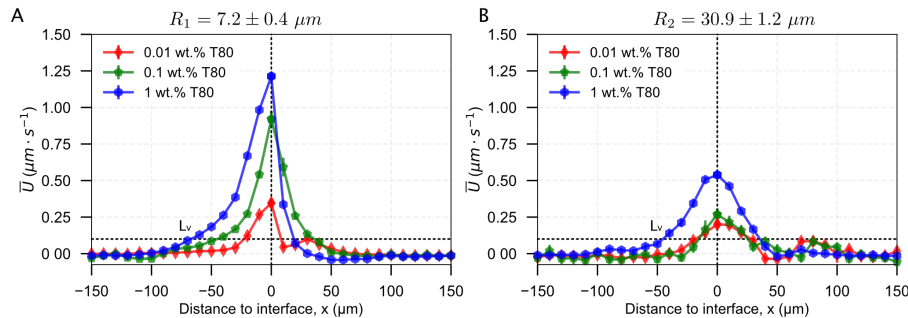


Figure 5: **Droplet dynamics in presence of 0.01, 0.1, and 1wt.% solute in solution, deduced from the droplet trajectories at $V_{sl} = 3 \mu m \cdot s^{-1}$.** Mean droplet velocity versus distance to interface for (A) $R_1 = 7.2 \pm 0.4 \mu m$ and (B) $R_2 = 30.9 \pm 1.2 \mu m$. The droplets accelerate as the solidification front approaches, and decelerate as they are engulfed into the ice. © (2020) S. Tyagi *et al.* (10.6084/m9.figshare.14815083) CC BY 4.0 license <https://creativecommons.org/licenses/by/4.0/>.

262 At large distances from the interface, larger than $100 \mu m$ the droplets in
 263 water are unperturbed and their mean velocity \bar{U} in the sample frame is zero.
 264 As they get closer to the interface, they start getting repelled. The mean droplet
 265 velocity (\bar{U}) increases and exhibits a maximum (U_{max}), when the leading edge
 266 of the droplets coincides with the initial position of the growing crystal. We note
 267 that the droplet velocity \bar{U} is lower than V_{sl} , which means that the droplets are
 268 finally captured in ice after a typical time, called interaction time (defined in
 269 Fig. S1), which is discussed later. As the droplets are captured in ice, their
 270 velocity \bar{U} returns to zero. As shown in Fig.5, \bar{U} decreases for a larger droplet
 271 size, while it increases with an increasing surfactant concentration.

272 In Fig.6, we report the evolution of the maximum velocity U_{max} with the
 273 surfactant concentration, the droplet size, and the solid liquid interface velocity
 274 V_{sl} . Similar to \bar{U} , we observe an increase of U_{max} with an increasing surfactant
 275 concentration and that the larger R_2 droplets get pushed away from the growing
 276 solid at lower velocities as compared to the smaller R_1 droplets. Furthermore,

277 increasing V_{sl} leads to a decrease of the U_{max} .

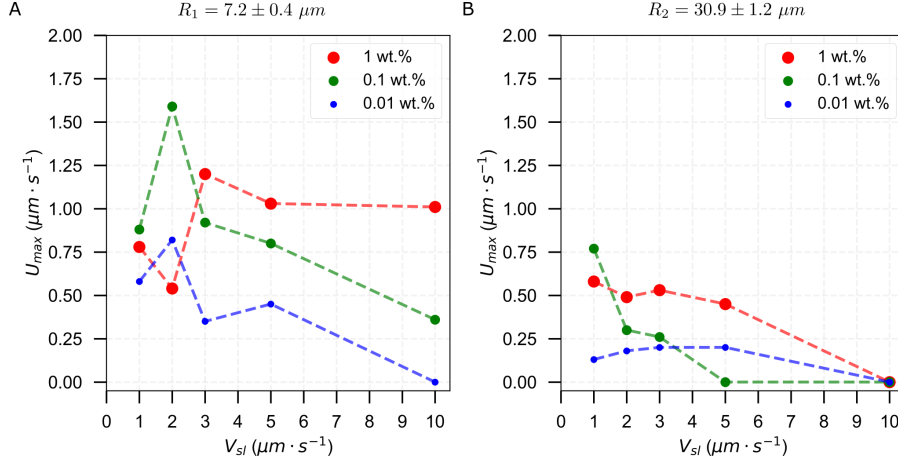


Figure 6: **Maximum mean droplet velocity (U_{max}) when the droplet front edge coincides with the ice-water interface (distance to interface = $0 \mu m$) for (A) $R_1 = 7.2 \pm 0.4 \mu m$ and (B) $R_2 = 30.9 \pm 1.2 \mu m$.** In general, the magnitude of U_{max} is greater for higher surfactant concentrations and smaller droplet sizes. An increasing growth rate V_{sl} as well as droplet radius promote a smaller magnitude of U_{max} . The dotted lines are for visualization and do not represent an extrapolation of the results denoted by the circular markers. © (2020) S. Tyagi *et al.* (10.6084/m9.figshare.14815083) CC BY 4.0 license <https://creativecommons.org/licenses/by/4.0/>.

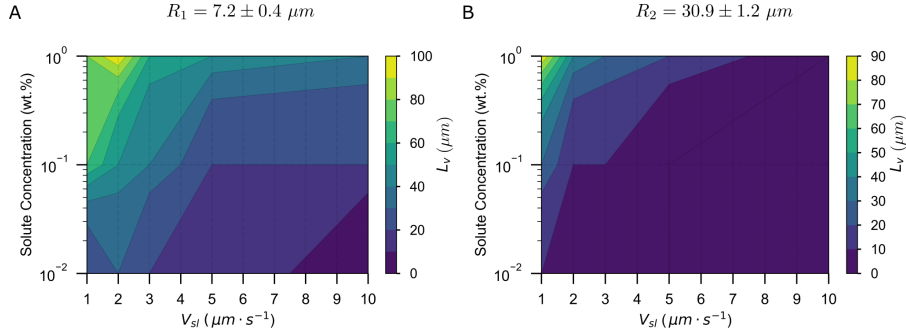


Figure 7: **Characteristic length scale L_v in the plane of Solute Concentration (wt.%) versus Solidification Velocity (V_{sl}).** Contour plots denoting the magnitude of L_v for (A) $R_1 = 7.2 \pm 0.4 \mu m$ and (B) $R_2 = 30.9 \pm 1.2 \mu m$. Each contour line denotes a constant magnitude of L_v equivalent to the value shown on the calibration bar. The distance L_v , where droplets in water start getting repelled by the interface, increases significantly with the solute concentration, while it decreases with an increasing growth rate. © (2020) S. Tyagi *et al.* (10.6084/m9.figshare.14815083) CC BY 4.0 license <https://creativecommons.org/licenses/by/4.0/>.

278 From the evolution of \bar{U} with the distance to the interface, we define a char-
 279 acteristic length scale, L_v , corresponding to the distance at which the droplets
 280 attain a mean velocity (\bar{U}) of $0.1 \mu m \cdot s^{-1}$, which is shown in Fig.7. This distance
 281 corresponds to the range of interaction between the droplets and the interface.
 282 We find that the droplets get repelled over distances ranging between 10 and
 283 $100 \mu m$, often larger than their diameter, especially for the largest surfactant
 284 concentrations. Smaller droplets with radius R_1 are repelled at greater distances
 285 from the interface as compared to the larger R_2 droplets. Increasing the growth
 286 rate decreases the characteristic distance L_v .

287 We also depict in Fig.8 the interaction time τ (defined in SI), which repre-
 288 sents the time during which the velocity of the droplets is different from zero
 289 before and after crossing the interface. In general, we notice that the interaction
 290 time diminishes with an increasing solidification velocity (V_{sl}) and reduces to
 291 zero at higher growth rates ($V_{sl} \geq 5 \mu m \cdot s^{-1}$), independent of the surfactant
 292 concentration. An interaction time of $0 s$ implies that the droplets get engulfed
 293 into the ice instantaneously and hence, are not repelled by the advancing solid-
 294 liquid interface. In contrast, the interaction time increases strongly with the
 295 surfactant concentration at relatively lower growth rates ($V_{sl} \leq 3 \mu m \cdot s^{-1}$).

296 In Fig.9 we present the droplet displacement δ due to their repulsion by the
 297 front (defined in Fig. S1), which represents the distance moved by the droplets
 298 during the interaction time. We again observe that increasing the surfactant
 299 concentration leads to higher displacements while increasing the growth rate
 300 leads to a lower displacement.

301 The results described so far emphasize that an increasing amount of surfac-
 302 tant induces a repulsion of the droplets by the interface over large distances,
 303 of the order ten to a hundred of microns away from the interface and that the
 304 droplet dynamics is influenced by the bulk surfactant concentration, the growth
 305 rate and the droplet size. These three parameters control the local gradient of
 306 surfactant concentration close to the solidification front. Indeed the surfactant
 307 concentration close to the solid-liquid interface is higher as compared to the

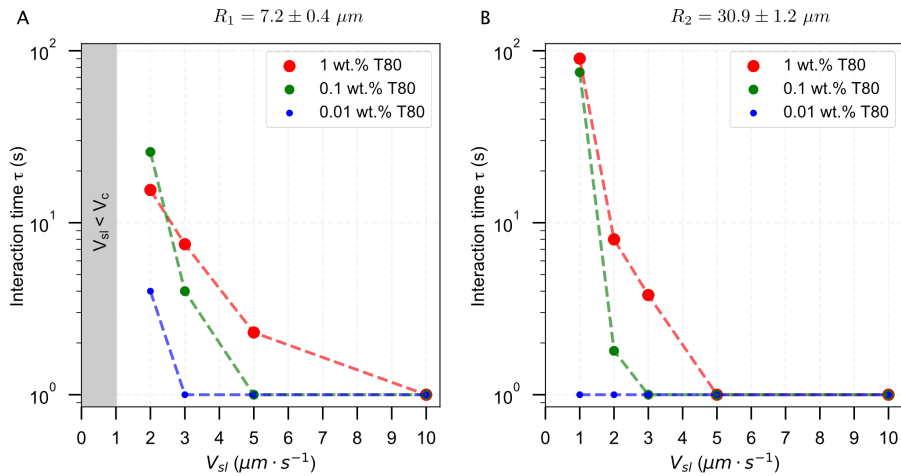


Figure 8: **Interaction time for oil droplets dispersed in water at three distinct solute concentrations.** Plot of characteristic interaction time for (A) $R_1 = 7.2 \pm 0.4 \mu\text{m}$ and (B) $R_2 = 30.9 \pm 1.2 \mu\text{m}$. Droplets tend to interact or feel the presence of an approaching ice-water interface during 10 to 100 s at high solute concentrations ($\geq 0.1 \text{ wt.}\%$) and low growth rates ($\leq 5 \mu\text{m} \cdot \text{s}^{-1}$). The dotted lines are for visualization and do not represent an extrapolation of the results denoted by the circular markers. © (2020) S. Tyagi *et al.* (10.6084/m9.figshare.14815083) CC BY 4.0 license <https://creativecommons.org/licenses/by/4.0/>.

308 bulk concentration far from the interface because of its low solubility in ice.
 309 For *steady-state* planar growth, the concentration field of rejected solutes in the
 310 remaining liquid writes

$$C_L = C_0 + C_0 \left(\frac{1 - K_0}{K_0} \right) \exp \left[\frac{-V_{sl}}{D} |x| \right] \quad (1)$$

311 where C_L is the solute concentration at a distance x from the interface, C_0
 312 is the bulk solute concentration in the liquid far from the interface, D is the
 313 solute diffusion coefficient and K_0 , the partition coefficient defined as the ratio
 314 of surfactant concentration in the solid phase to the one in the liquid [36].

315 In a previous article [19], we suggested that the displacement of the droplets
 316 is caused by surfactant concentration gradients close to the ice-water interface,
 317 possibly through a phenomenon called diffusiophoresis [37]. Diffusiophoresis
 318 is provoked by solute concentration gradients and can lead to displacement of

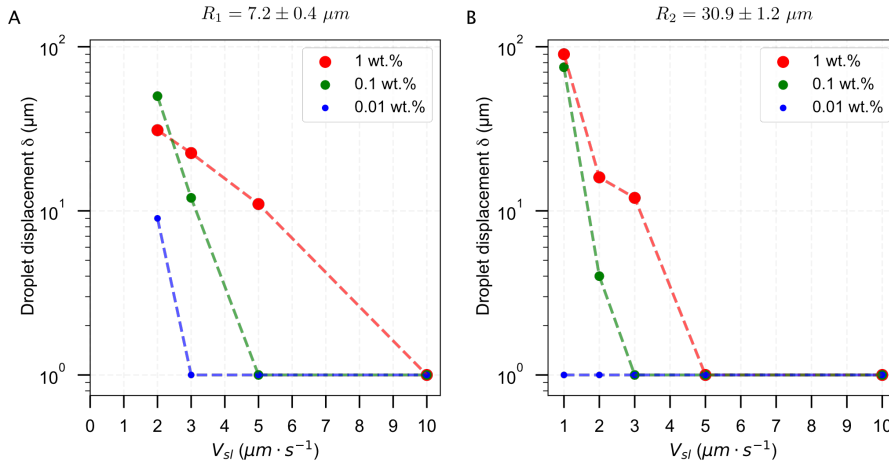


Figure 9: **Displacement of oil droplets dispersed in water at three distinct solute concentrations, while interacting with the ice-water interface.** Plot of droplet displacement for (A) $R_1 = 7.2 \pm 0.4 \mu\text{m}$ and (B) $R_2 = 30.9 \pm 1.2 \mu\text{m}$. The interaction of droplets with an advancing ice-water interface can displace them by increasing distances ($\geq 10 \mu\text{m}$) owing to a high amount of surfactant ($\geq 0.1 \text{ wt.}\%$) in the bulk solution. The dotted lines are for visualization and do not represent an extrapolation of the results denoted by the circular markers. © (2020) S. Tyagi *et al.* (10.6084/m9.figshare.14815083) CC BY 4.0 license <https://creativecommons.org/licenses/by/4.0/>.

319 micrometric particles with velocities of the order of a few micron per second,
 320 comparable to the droplet velocities that we measure in our study. From Eq. (1),
 321 it is expected that the local gradient of surfactant concentration spans over a
 322 typical distance $L_d = D/V_{sl}$ [36]. Hence an increasing growth rate (V_{sl}) will de-
 323 crease the distance at which the solute field can be perceived by the droplets and
 324 can qualitatively account for the decreasing values of L_v measured (see Fig.7)
 325 at high growth rates ($V_{sl} \geq 5 \mu\text{m} \cdot \text{s}^{-1}$). Moreover the concentration gradient
 326 $C_L - C_0$ depends linearly on C_0 which can possibly account for the strong influ-
 327 ence of the surfactant concentration on the droplet displacement. We note that
 328 diffusiphoretic displacements of particles have been studied theoretically and
 329 experimentally for simple solutes such as ionic salts, dissolved gas or charged
 330 surfactants such as Sodium dodecylSulfate [37–40] but was never reported for
 331 non-ionic species.

332 To further study the influence of the surfactant concentration gradients on

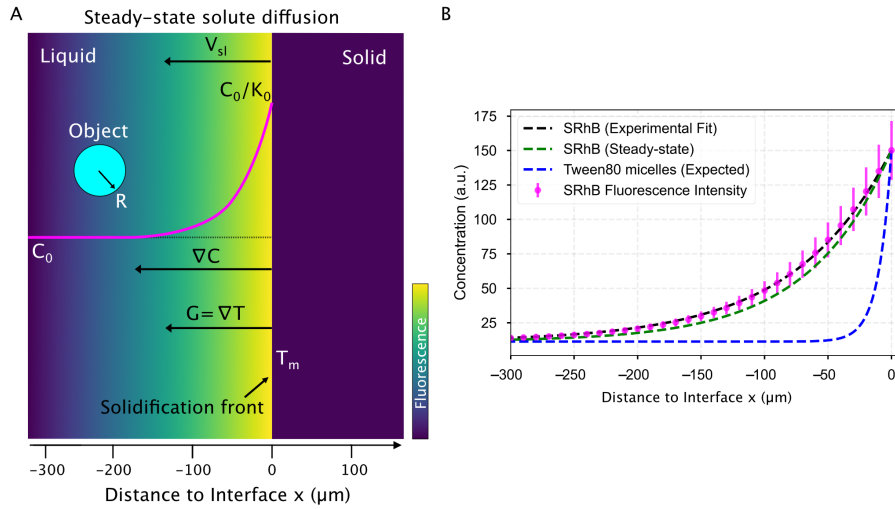


Figure 10: **Solute rejected by the growing solid phase and segregated at the solid-liquid interface during *steady-state* directional solidification.** (A) Model sketch depicting the concentration profile evolution of a solute (in magenta) in the remaining liquid, rejected by a solidification front advancing at V_{sl} , during *steady-state* planar growth. (B) Mean fluorescence intensity (magenta) of SRhB, acquired using a confocal microscope, is fit with a theoretical diffusion-type exponential (black line). The predicted *steady-state* diffusion of SRhB (green line), using the model from Tiller *et al.* [36], corresponds closely to the experimental data fit. A *steady-state* planar growth is thus verified. The corresponding *steady-state* diffusion profile of Tween 80 micelles (blue) shows a significant difference in length scales over which the two molecules (SRhB and Tween 80) diffuse. All data presented was recorded for a growth rate of $3 \mu\text{m} \cdot \text{s}^{-1}$. © (2020) S. Tyagi *et al.* (10.6084/m9.figshare.14815083) CC BY 4.0 license <https://creativecommons.org/licenses/by/4.0/>.

333 the droplet dynamics, it would be useful to measure *in situ* the surfactant
 334 concentration close to the front. However Tween 80 does not fluoresce, hence
 335 we cannot measure its concentration profile. However it is in principle possible
 336 to predict it from Equation 1 provided a steady state regime is reached in our
 337 experiments. Therefore we examine the validity of Equation 1 by recording the
 338 fluorescence intensity of the dye, SRhB, which can be obtained easily with the
 339 confocal microscope (see Fig.10A). The concentration profile of SRhB rejected
 340 by the ice-water interface, deduced from the fluorescence intensity profile for a
 341 growth rate of $3 \mu\text{m} \cdot \text{s}^{-1}$ is given in Fig.10B. At $3 \mu\text{m} \cdot \text{s}^{-1}$, the concentration
 342 profile obtained is in agreement with the *steady-state* diffusion profile predicted

343 from Eq.1 (see Fig.10B). However we note that the *steady-state* approximation
344 is not valid at higher velocities (not shown) probably because constitutional
345 undercooling modifies the local temperature of the front hence the diffusion
346 coefficient of the dye.

347 Interestingly, we see from Fig.10B which is obtained for a velocity of $3 \mu m \cdot$
348 s^{-1} , that the distance at which the dye concentration profile starts increasing is
349 of the order of $150 \mu m$. This value is much higher than the typical distance L_v
350 over which both the large and small droplets get repelled from the interface at
351 the same velocity, ranging between 40 and $80 \mu m$ depending on the surfactant
352 concentration and the droplet size. As the surfactant monomers and the dye
353 have the same diffusion coefficient, we would expect that the distance L_d is
354 similar for both species.

355 To account for the discrepancy between the measured values of L_v and the
356 theoretical $L_d = D/V_{sl}$, one may suggest that the droplet dynamics may be
357 controlled by the concentration gradient of surfactant micelles, which diffusion
358 coefficient is lower than that of the monomers and for which we expect a lower
359 value of L_d . Using DLS, we measured the diffusion coefficient of the micelles
360 and calculated the corresponding concentration profile using Eq.1. As shown
361 in Fig.10B, at a growth rate of $3 \mu m \cdot s^{-1}$, we obtain a typical distance L_d of
362 $10 \mu m$, which is lower than the distance L_v measured experimentally at this
363 growth rate. Hence it turns out that the experimentally measured value of L_v
364 ranges between the L_d values calculated either for the surfactant micelles or for
365 the monomers. However we note that the monomer and micelle concentration
366 profiles close to ice-water front depends on the exchange dynamics between the
367 surfactants and the micelles, hence may not be at equilibrium.

368 **3.2 Droplets at the interface**

369 We now focus on the behaviour of droplets when they come in contact (distance
370 to interface = $0 \mu m$) with the solid-liquid interface. We observe three typical
371 behaviours of oil droplets as they encounter an approaching front, as shown

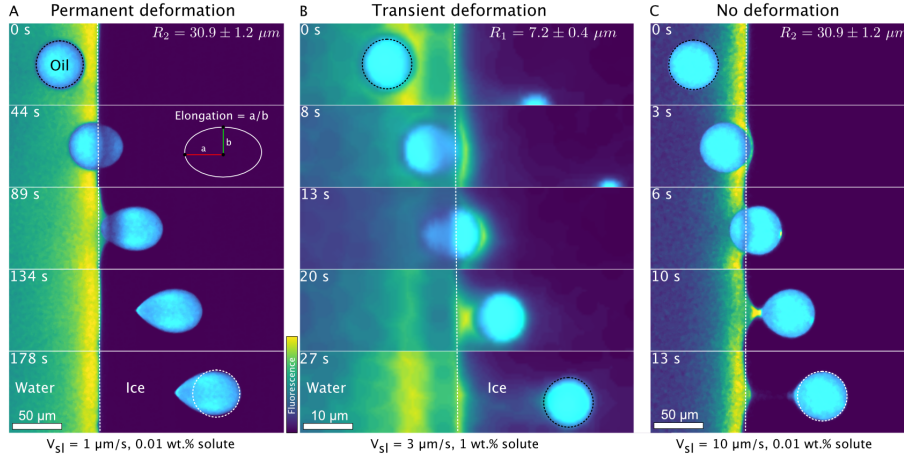


Figure 11: **Typical time-lapse montage depicting the three types of deformation behaviour of oil droplets while undergoing directional planar front solidification.** (A) The droplets elongate at the ice-water interface and remain deformed in the ice phase, scale bar = $50 \mu m$ (B) The droplets deform in a transient manner ($t = 13 s$) at the ice-water interface and recover their shape as they are captured by the growing ice phase, scale bar = $10 \mu m$ (C) The droplets do not undergo deformation and preserve their shape during their interaction and further engulfment in the growing crystal. Scale bar = $50 \mu m$. Oil is in cyan, water is in colormap viridis (fluorescence bar), and ice is in black. © (2020) S. Tyagi *et al.* (10.6084/m9.figshare.14815083) CC BY 4.0 license <https://creativecommons.org/licenses/by/4.0/>.

372 in Fig.11. The droplets can elongate permanently as they get engulfed in the
 373 growing ice (Fig.11A), the droplets may deform transiently ($t = 13 s$) at the
 374 ice-water interface and subsequently relax to their original spherical shape as
 375 they move further into the ice phase (Fig.11B), or the droplets remain mostly
 376 spherical during their engulfment by the growing crystal (Fig.11C). We notice
 377 that the deformation behaviour depends on the droplet size R , the imposed
 378 growth rate V_{sl} , and the bulk surfactant concentration. Therefore, we need to
 379 systematically study the effect of these solidification parameters to understand
 380 the different types of deformation observed.

381 The droplet deformation is estimated from the analysis of $2D$ shape elonga-
 382 tion, as shown in the schematic in Fig.11A, taking the ratio of droplet diameters
 383 along \vec{x} and \vec{y} . In Fig.12, we depict the mean elongation profiles calculated for
 384 50 to 400 (depending on R and V_{sl}) droplet interactions in $0.01 wt. \%$ and $1 wt. \%$

385 solute solution at varying growth rates for two different droplet sizes (R_1, R_2).

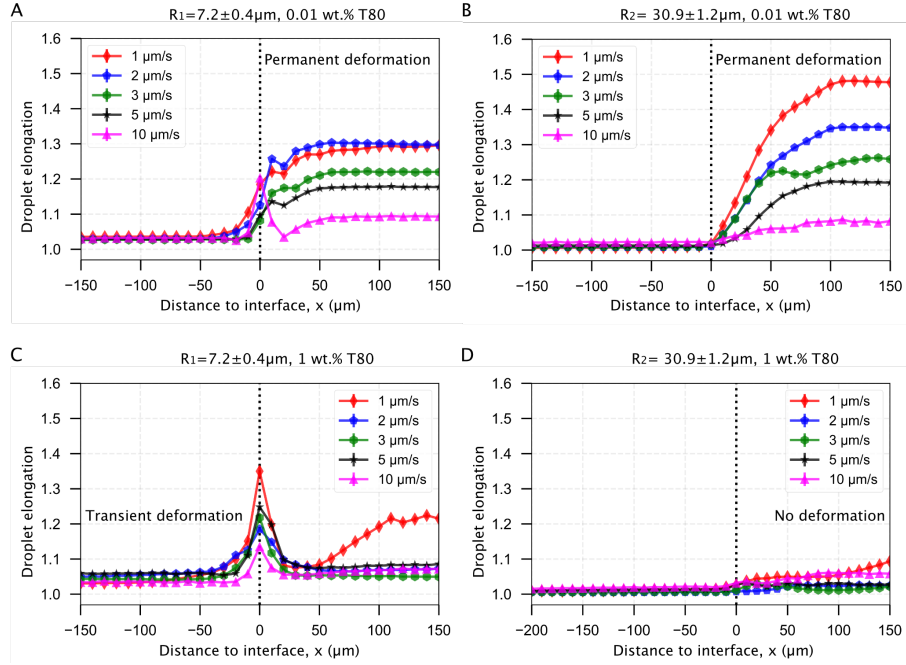


Figure 12: **Mean elongation profiles for oil droplets encountering an approaching ice-water interface.** Planar solidification front induced permanent deformation of oil droplets dispersed in a solution with (A,B) 0.01 wt.% solute concentration having a size of (A) $R_1 = 7.2 \pm 0.4 \mu\text{m}$ (B) $R_2 = 30.9 \pm 1.2 \mu\text{m}$. The transient and no deformation regimes for droplets in (C,D) 1 wt.% solute concentration having a size of (C) $R_1 = 7.2 \pm 0.4 \mu\text{m}$ (D) $R_2 = 30.9 \pm 1.2 \mu\text{m}$. © (2020) S. Tyagi *et al.* (10.6084/m9.figshare.14815083) CC BY 4.0 license <https://creativecommons.org/licenses/by/4.0/>.

386 We observe from Fig.12A and Fig.12B that the droplets undergo permanent
 387 elongation for the two droplet sizes (R_1, R_2), when the bulk surfactant concen-
 388 tration is 0.01 wt.%. The elongation is ≈ 1.0 , representing a circle, when the
 389 droplets are in the remaining liquid far from the interface. The droplets start
 390 getting elongated as their front edge touches the interface (distance = 0 μm)
 391 and their shape transforms into an ellipse (elongation > 1.0). The droplet de-
 392 formation evolves further and reaches a constant magnitude when the front edge
 393 is located at a distance of $2R \times Elongation$. Once the droplets are completely
 394 engulfed in the ice, their shape does not evolve any more (Fig.12A,B). Interest-
 395 ingly, we notice that the elongation reduces with an increasing growth rate for

396 both the droplet sizes investigated. However, the maximum elongation for the
397 smaller R_1 droplets is lower as compared to the larger R_2 droplets at the given
398 0.01 *wt.%* solute concentration.

399 In Fig.12C, we report the transient deformation of the oil droplets as they
400 confront the ice-water interface with 1 *wt.%* bulk solute concentration. Here,
401 the oil droplets undergo elongation at the interface (distance =0 μm) but even-
402 tually recover their shape as they are completely engulfed in the ice. In contrast,
403 from Fig.12D we notice that the larger R_2 droplets do not undergo any type
404 of deformation at the same solute concentration of 1 *wt.%*. Hence, the elon-
405 gation profile of R_2 droplets remains unmodified during the droplet-interface
406 confrontation.

407 We deduce from these observations that the droplets confronting an ap-
408 proaching interface have distinct behaviours depending on the concentration of
409 solute in the bulk solution. In particular, an increasing solute concentration
410 tends to decrease the droplet elongation significantly.

411 Several experimental and theoretical studies devoted to the shape of bubbles
412 during solidification in the absence of surfactant can be found in the literature
413 [41–43]. Highly elongated bubbles along with the formation of a highly curved
414 tip at the bubble-ice interface were observed [41, 42] and are controlled by
415 the contact angle between the bubbles and the ice-water interface [43]. In
416 the case of the low surfactant concentrations, we see from Fig.11A that the
417 contact angle between the droplets and the ice-water interface remains close to
418 90° during engulfment, similarly to bubbles, because of the weak thermal flux
419 in the droplets owed to their low thermal conductivity in comparison to water
420 [44]. This results in tear-shaped drops which are very similar to those reported
421 in the literature for bubbles.

422 At higher surfactant concentration we observe much lower elongations. Ac-
423 cording to Eq.1, an increasing bulk solute concentration (C_0) implies a higher
424 concentration of the solute segregated (C_0/K_0) at the solid-liquid interface. The
425 segregation of solute is further enhanced owing to an obstruction of their diffu-

426 sion field by the droplets in the vicinity of the solid-liquid interface [13, 45]. The
 427 segregated solute, trapped in the layer between the droplet and the interface,
 428 induces solute premelting [46, 47] (Fig.4B at $t = 44$ s, Fig.11B at $t = 8$ s, in
 429 Fig.11C at $t = 3$ s) which in turn causes a lowering of the equilibrium melt-
 430 ing temperature of water. Therefore these premelted films are stable below the
 431 solid's bulk melting temperature, T_m and the thickness of the premelted films
 432 increases with the solute concentration [18, 46]. As a premelting film interca-
 433 lates between the droplets and the solid liquid interface, the situation is very
 434 different from the literature studies discussed above as no finite contact angle
 435 between the drops and the interface can be defined. Here we suggest that the
 436 liquid-liquid interfacial tension between the droplet and the premelting film fa-
 437 vors spherical shapes to minimize the interfacial area. Interestingly we note that
 438 the effect of size is different at low and high surfactant concentrations. At low
 439 surfactant concentrations, smaller droplets undergo a lower deformation, prob-
 440 ably because of a higher capillary pressure inside the drops that opposes the
 441 deformation. At opposite, for large surfactant concentrations, smaller droplets
 442 present a transient deformation, while larger droplets remain mostly spheri-
 443 cal. This effect may be linked to the stronger segregation of solute in the films
 444 between the droplets and the ice in the case of larger films.

445 3.3 Droplets in Ice

446 We have discussed so far the dynamics and consequences of oil droplets interact-
 447 ing with an approaching ice-water interface. In the last section, we investigate
 448 the fate of droplets after their engulfment by the ice front.

449 At 1 wt.% solute in the aqueous solution, at a growth rate of $1 \mu\text{m} \cdot \text{s}^{-1}$, the
 450 droplets undergo an elongation process after engulfment whereby the two radii,
 451 along \vec{x} and \vec{y} , are stretched in magnitude as the droplets progress further in
 452 ice. This means that the droplets flatten in the z direction as they are engulfed
 453 in the ice. We depict this phenomenon with a time-lapse montage, highlighting
 454 the deformation, in Fig.13. Interestingly, we observe this phenomenon only at

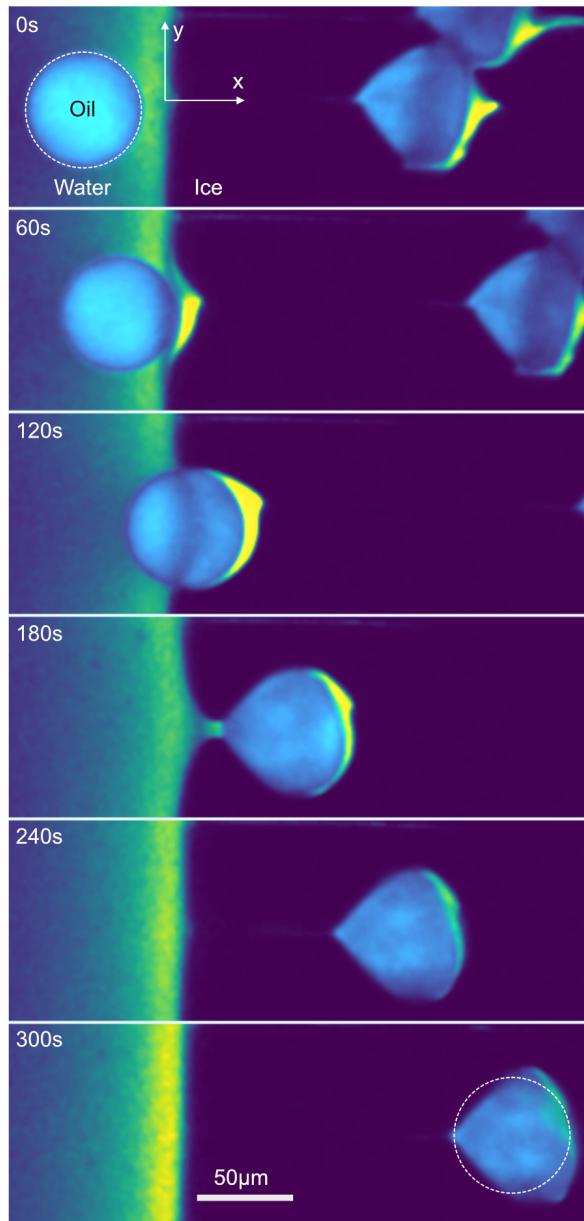


Figure 13: **Crushing of oil droplets during their engulfment in ice at a growth rate of $V_{sl} = 1 \mu\text{m}\cdot\text{s}^{-1}$ with 1 wt% solute in solution. $R_2 = 30.9 \pm 1.2 \mu\text{m}$.** Typical time-lapse montage depicting the crushing of an oil droplet, scale bar = $50 \mu\text{m}$. The dashed circle indicate the shape of the droplet before encapsulation. Note that in the crushing regime, the droplets are elongated in a direction parallel to the front, unlike in the other regimes (elongation perpendicular to the front). © (2020) S. Tyagi *et al.* (10.6084/m9.figshare.14815083) CC BY 4.0 license <https://creativecommons.org/licenses/by/4.0/>.

455 a growth rate of $1 \mu\text{m} \cdot \text{s}^{-1}$ in the presence of 1 *wt.*% bulk solute concentration
456 for both droplets radii R1 and R2.

457 We currently have no definitive explanations for this behavior. One possibil-
458 ity could be that the shape of the water/ice meniscus in these conditions (curved
459 meniscus) may favor entrapment and flattening of the droplets between the ice
460 and the glass surface. However, this particular point would deserve additional
461 experiments, in particular in 3D, which are beyond the scope of the current
462 study.

463 Furthermore we note that once the droplets are trapped in the ice, we do
464 not observe any thermal regelation, i.e the droplets do not manifest any motion
465 relative to the ice. Moreover the liquid layer between the droplet from the
466 growing solid decreases in thickness as the droplets move along the temperature
467 gradient in ice towards an increasing undercooling ($\Delta T = T_m - T$, where T is
468 the temperature of the substrate) [1]. The study of particle migration in ice is an
469 important topic of research to understand frost heave, glacier motion, and ice-
470 core dating among other technological applications [1]. Recent studies suggest
471 that the presence of impurities or solutes tend to accelerate the *regelation* of
472 trapped particles in ice. Typical migration velocities of $0.1 \mu\text{m} \cdot \text{s}^{-1}$ at ΔT of 1 *K*
473 have been reported for micron sized particles in the presence of impurities [48].
474 Another recent study highlights the major impact of impurities on the rapid
475 displacement (0.5 *cm*) over small time scales (120 *s*) of 1 μm silicon particles
476 trapped in ice [49]. The objects investigated here are 1 order of magnitude (or
477 more) larger, which could explain why no regelation was observed. The use of
478 cryo-confocal microscopy with the ability to image the solute segregation has
479 a promising prospect for investigating such mechanisms. We believe the high
480 space and temporal resolution can be used effectively to resolve the dynamics
481 of individual colloidal particles to gain further insight into *regelation*.

482 4 Conclusions

483 In the first section, we have investigated the role of solutes on the dynamics of
484 freezing oil droplets using *in situ* cryo-confocal microscopy. We have reported
485 on the significant magnitude of droplet-front interaction time and the resulting
486 droplet displacement owing to the solute effects. We believe this can be an
487 important criterion for controlling the spatial distribution of objects, especially
488 in multiple object scenarios. The control of the material microstructure has
489 been a topic of interest in alloy solidification (especially in particle-reinforced-
490 composites) and for impurity control in castings and single crystal growth. The
491 object dynamics and impact of solute (or impurity) are still complex to quantify
492 as the observation of solidification *in situ* remains challenging. We have tried
493 to advance towards an *in situ* quantification of the solute mechanisms at play
494 and further work is required to correlate the dye fluorescence intensity to the
495 absolute solute concentration gradient. The latter can be useful in predicting
496 thermal convection and non *steady-state* solidification regimes.

497 In the second section, we have shown that the deformation of droplets at
498 the ice-water interface depends strongly on the growth rate (V_{sl}) and the cor-
499 responding bulk solute concentration (C_0). Furthermore, the addition of solute
500 increases the thickness of the observable premelted films, which appears to act
501 as a protection mechanism against the interface initiated droplet deformation.
502 The local solute environment and deformation are two important criterion for
503 cryopreservation in particular. In cryobiology, the excess of solute causes severe
504 osmotic stresses that can instigate cell membrane rupture and hence, cryoinjury
505 to cells and tissues [4, 12]. In food engineering, alterations to the continuous
506 phase concentration or to the shape and size of dispersed droplets is detrimen-
507 tal to the freeze-thaw stability of consumable emulsions [8]. Hence, a complete
508 understanding of the solute redistribution mechanisms along with the associ-
509 ated object deformation at the corresponding freezing conditions is desired.
510 Our multi-dimensional approach highlights the importance of different solidifi-

511 cation parameters and the ubiquitous role of solute in dominating the various
512 aspects of object deformation behaviour. Further work is required to accurately
513 estimate the direction and magnitude of forces at the origin of the observed
514 deformation.

515 In conclusion, we report that the oil droplets undergoing directional solidifi-
516 cation feel the impact of solute at every stage, from being in the liquid phase to
517 getting captured by the growing ice-water interface. The solute plays an impor-
518 tant role in determining the droplet shape (deformed or not), droplet behaviour
519 (engulfment or rejection), and eventually the droplet spatial distribution. To
520 predict the solidified microstructure, an understanding of the several in-situ
521 mechanisms at play is therefore indispensable. The use of rapid cryo-confocal
522 microscopy facilitates an *in situ* investigation and quantification of solidifica-
523 tion mechanisms with visualization of the local solute segregation. To represent
524 the observations in real-life systems, we need to explore models incorporating
525 interaction dynamics and object behaviour with solute effects. Current theories
526 do not encompass all the factors required for explaining the long-range solute
527 effects on the objects during solidification. We hope our experimental data can
528 serve to improve the existing theoretical models. Finally, we suggest that the
529 freezing of oil-in-water emulsions may serve as an analogue for studying the *in*
530 *situ* interaction of foreign objects with an advancing solid-liquid interface in the
531 presence of solute effects.

532 **Acknowledgements**

533 The research leading to these results has received funding from the ANRT and
534 Saint-Gobain through a CIFRE fellowship (N° 2017/0774). We would like to
535 thank Alban Sauret and Virgile Thievenaz for discussing the deformation of
536 droplets.

537 **Author contributions**

538 S.D. and C.M. designed and supervised the project, S.D, C.M. and S.T. designed
539 the experiments, S.T. carried out the confocal microscopy, S.T., C.M. and S.D.
540 analyzed the data. All authors discussed the results and implications and wrote
541 the manuscript.

542 **Corresponding Authors**

543 Correspondence should be sent to Cécile Monteux (Cecile.Monteux@espci.fr)
544 and Sylvain Deville (sylvain.deville@univ-lyon1.fr)

545 **Conflict of interest**

546 The authors declare no conflict of interest.

547 **Availability of materials and data**

548 The datasets generated during and/or analysed during the current study are
549 available from the corresponding author on reasonable request.

550 **References**

- 551 [1] J. G. Dash, A. W. Rempel, and J. S. Wettlaufer. The physics of pre-
552 melted ice and its geophysical consequences. *Reviews of Modern Physics*,
553 78(3):695–741, 2006.
- 554 [2] M Shafiur Rahman. *Handbook of food preservation*. CRC press, 2007.
- 555 [3] VL Bronstein, YA Itkin, and GS Ishkov. Rejection and capture of cells
556 by ice crystals on freezing aqueous solutions. *Journal of Crystal Growth*,
557 52:345–349, 1981.

- 558 [4] C Körber. Phenomena at the advancing ice-liquid interface: solutes, parti-
559 cles and biological cells. *Quarterly reviews of biophysics*, 21:229–298, 1988.
- 560 [5] Lifeng Zhang. Nucleation, growth, transport, and entrapment of inclusions
561 during steel casting. *Jom*, 65(9):1138–1144, 2013.
- 562 [6] H Li, EA Ghezal, A Nehari, G Alombert-Goget, A Brenier, and K Lebbou.
563 Bubbles defects distribution in sapphire bulk crystals grown by czochralski
564 technique. *Optical Materials*, 35(5):1071–1076, 2013.
- 565 [7] Sylvain Deville. Freeze-casting of porous ceramics: a review of current
566 achievements and issues. *Advanced Engineering Materials*, 10(3):155–169,
567 2008.
- 568 [8] Supratim Ghosh and John N Coupland. Factors affecting the freeze-thaw
569 stability of emulsions. *Food Hydrocolloids*, 22(1):105–111, 2008.
- 570 [9] OM Bunoiu, Th Duffar, and I Nicoara. Gas bubbles in shaped sapphire.
571 *Progress in crystal growth and characterization of materials*, 56(3-4):123–
572 145, 2010.
- 573 [10] D. Shangguan, S. Ahuja, and D. M. Stefanescu. An analytical model for
574 the interaction between an insoluble particle and an advancing solid/liquid
575 interface. *Metallurgical Transactions A*, 23(2):669–680, 1992.
- 576 [11] R. Asthana and S. N. Tewari. The engulfment of foreign particles by a
577 freezing interface. *Journal of Materials Science*, 28(20):5414–5425, 1993.
- 578 [12] Gregory M. Fahy. The relevance of cryoprotectant "toxicity" to cryobiology.
579 *Cryobiology*, 23(1):1–13, 1986.
- 580 [13] J. K. Kim and P. K. Rohatgi. The effect of the diffusion of solute between
581 the particle and the interface on the particle pushing phenomena. *Acta*
582 *Materialia*, 46(4):1115–1123, 1998.

- 583 [14] Adrian V. Catalina, Subhayu Sen, Doru M. Stefanescu, and William F.
584 Kaukler. Interaction of porosity with a planar solid/liquid interface. *Met-*
585 *allurgical and Materials Transactions A*, 35(5):1525–1538, 2004.
- 586 [15] Sidhanth Tyagi, Hélène Huynh, Cécile Monteux, and Sylvain Deville. Ob-
587 jects interacting with solidification fronts: Thermal and solute effects. *Ma-*
588 *terialia*, 12(April):100802, 2020.
- 589 [16] Justin C. T. Kao and Alexander A. Golovin. Particle capture in binary
590 solidification. *Journal of Fluid Mechanics*, 625(September 2008):299, 2009.
- 591 [17] Yi Yang, JW Garvin, and HS Udaykumar. Sharp interface numerical simu-
592 lation of directional solidification of binary alloy in the presence of a ceramic
593 particle. *International journal of heat and mass transfer*, 51(1-2):155–168,
594 2008.
- 595 [18] JS Wettlaufer and M Grae Worster. Premelting dynamics. *Annu. Rev.*
596 *Fluid Mech.*, 38:427–452, 2006.
- 597 [19] Dmytro Dedovets, Cécile Monteux, and Sylvain Deville. Five-dimensional
598 imaging of freezing emulsions with solute effects. *Science*, 360(6386):303–
599 306, 2018.
- 600 [20] J. A. Sekhar and R. Trivedi. Solidification microstructure evolution in the
601 presence of inert particles. *Materials Science and Engineering A*, 147(1):9–
602 21, 1991.
- 603 [21] Jürgen Pötschke and Volker Rogge. On the behaviour of foreign particles at
604 an advancing solid-liquid interface. *Journal of Crystal Growth*, 94(3):726–
605 738, 1989.
- 606 [22] A. W. Rempel and M. G. Worster. Interaction between a particle and an
607 advancing solidification front. *Journal of Crystal Growth*, 205(3):427–440,
608 1999.

- 609 [23] A. W. Rempel and M. G. Worster. Particle trapping at an advancing
610 solidification front with interfacial-curvature effects. *Journal of Crystal
611 Growth*, 223(3):420–432, 2001.
- 612 [24] Min S. Park, Alexander A. Golovin, and Stephen H. Davis. The encapsula-
613 tion of particles and bubbles by an advancing solidification front. *Journal
614 of Fluid Mechanics*, 560:415–436, 2006.
- 615 [25] P. S. Wei and S.Y. Y. Hsiao. Pore shape development from a bubble cap-
616 tured by a solidification front. *Int. J. Heat Mass Transf.*, 55(25-26):8129–
617 8138, dec 2012.
- 618 [26] E. A. Ghezal, H. Li, A. Nehari, G. Alombert-Goget, A. Brenier, K. Leb-
619 bou, M. F. Joubert, and M. T. Soltani. Effect of pulling rate on bubbles
620 distribution in sapphire crystals grown by the micropulling down (μ -PD)
621 technique. *Crystal Growth and Design*, 12(8):4098–4103, 2012.
- 622 [27] H. Jamgotchian, R. Trivedi, and B. Billia. Interface dynamics and cou-
623 pled growth in directional solidification in presence of bubbles. *Journal of
624 Crystal Growth*, 134(3-4):181–195, 1993.
- 625 [28] S. Sen, W. F. Kaukler, P. Curreli, and D. M. Stefanescu. Dynamics of
626 solid/liquid interface shape evolution near an insoluble particle - An X-ray
627 transmission microscopy investigation. *Metallurgical and Materials Trans-
628 actions A: Physical Metallurgy and Materials Science*, 28(10):2129–2135,
629 1997.
- 630 [29] F López Arbeloa, P Ruiz Ojeda, and I López Arbeloa. Fluorescence self-
631 quenching of the molecular forms of rhodamine b in aqueous and ethanolic
632 solutions. *Journal of luminescence*, 44(1-2):105–112, 1989.
- 633 [30] Rex Malcolm Chaplin Dawson, Daphne C Elliott, William H Elliott, and
634 Kenneth M Jones. *Data for biochemical research*, volume 3. Clarendon
635 Press, 2002.

- 636 [31] Eleanor LV Harris, S Angal, and Simon Roe. *Protein purification applica-*
637 *tions: a practical approach*, volume 71. IRL press Oxford, 1990.
- 638 [32] Alan D McNaught, Andrew Wilkinson, et al. *Compendium of chemical*
639 *terminology*, volume 1669. Blackwell Science Oxford, 1997.
- 640 [33] Johannes Schindelin, Ignacio Arganda-Carreras, Erwin Frise, Verena
641 Kaynig, Mark Longair, Tobias Pietzsch, Stephan Preibisch, Curtis Rueden,
642 Stephan Saalfeld, Benjamin Schmid, et al. Fiji: an open-source platform
643 for biological-image analysis. *Nature methods*, 9(7):676, 2012.
- 644 [34] Stéfan van der Walt, Johannes L. Schönberger, Juan Nunez-Iglesias,
645 François Boulogne, Joshua D. Warner, Neil Yager, Emmanuelle Guillard,
646 Tony Yu, and the scikit-image contributors. scikit-image: image processing
647 in Python. *PeerJ*, 2:e453, 6 2014.
- 648 [35] Dmytro Dedovets, Cécile Monteux, and Sylvain Deville. A temperature-
649 controlled stage for laser scanning confocal microscopy and case studies in
650 materials science. *Ultramicroscopy*, 195(August):1–11, 2018.
- 651 [36] W. A. Tiller, K. A. Jackson, J. W. Rutter, and B. Chalmers. The redistribu-
652 tion of solute atoms during the solidification of metals. *Acta Metallurgica*,
653 1(4):428–437, 1953.
- 654 [37] JL Anderson, ME Lowell, and DC Prieve. Motion of a particle generated by
655 chemical gradients. part 1. non-electrolytes. *J. Fluid Mech*, 117(1):107–121,
656 1982.
- 657 [38] Rodrigo Nery-Azevedo, Anirudha Banerjee, and Todd M Squires. Diffusio-
658 phoresis in ionic surfactant gradients. *Langmuir*, 33(38):9694–9702, 2017.
- 659 [39] Trevor J Shimokusu, Vanessa G Maybruck, Jesse T Ault, and Sang-
660 woo Shin. Colloid separation by co2-induced diffusiophoresis. *Langmuir*,
661 36(25):7032–7038, 2019.

- 662 [40] Suin Shim and Howard A Stone. Co₂-leakage-driven diffusiophoresis causes
663 spontaneous accumulation of charged materials in channel flow. *Proceedings*
664 *of the National Academy of Sciences*, 117(42):25985–25990, 2020.
- 665 [41] P. S. Wei, C.C. Huang, Z.P. Wang, K.Y. Chen, and C.H. Lin. Growths
666 of bubble/pore sizes in solid during solidification—an in situ measurement
667 and analysis. *J. Cryst. Growth*, 270(3-4):662–673, 2004.
- 668 [42] Norizaku Maeno. Air bubble formation in ice crystals. *Phys. Snow Ice*
669 *Proc.*, 1(1):207–2181, 1967.
- 670 [43] P. S. Wei and C.Y Ho. An Analytical Self-Consistent Determination of a
671 Bubble with a Deformed Cap Trapped in Solid during Solidification. *Metall.*
672 *Mater. Trans. B*, 33(February):91–100, 2002.
- 673 [44] AA Chernov, DE Temkin, and AM Mel’Nikova. The influence of the ther-
674 mal conductivity of a macroparticle on its capture by a crystal growing
675 from a melt. *Sov. Phys. Crystallogr.*, 22(6):656–658, 1977.
- 676 [45] R. Sasikumar and T. R. Ramamohan. Distortion of the temperature and
677 solute concentration fields due to the presence of particles at the solidifi-
678 cation front-effects on particle pushing. *Acta Metallurgica Et Materialia*,
679 39(4):517–522, 1991.
- 680 [46] J. Wettlaufer. Impurity Effects in the Premelting of Ice. *Physical Review*
681 *Letters*, 82(12):2516–2519, 1999.
- 682 [47] A. W. Rempel, J. S. Wettlaufer, and M. G. Worster. Interfacial Premelt-
683 ing and the Thermomolecular Force: Thermodynamic Buoyancy. *Physical*
684 *Review Letters*, 87(8):088501, 2001.
- 685 [48] Julia Schollick. *Real space study of pattern formation in freezing colloidal*
686 *suspensions*. PhD thesis, University of Oxford, 2012.
- 687 [49] Navaneeth K. Marath and J. S. Wettlaufer. Impurity effects in thermal
688 regelation. *Soft Matter*, 16(25):5886–5891, 2020.

5 Supplementary Information

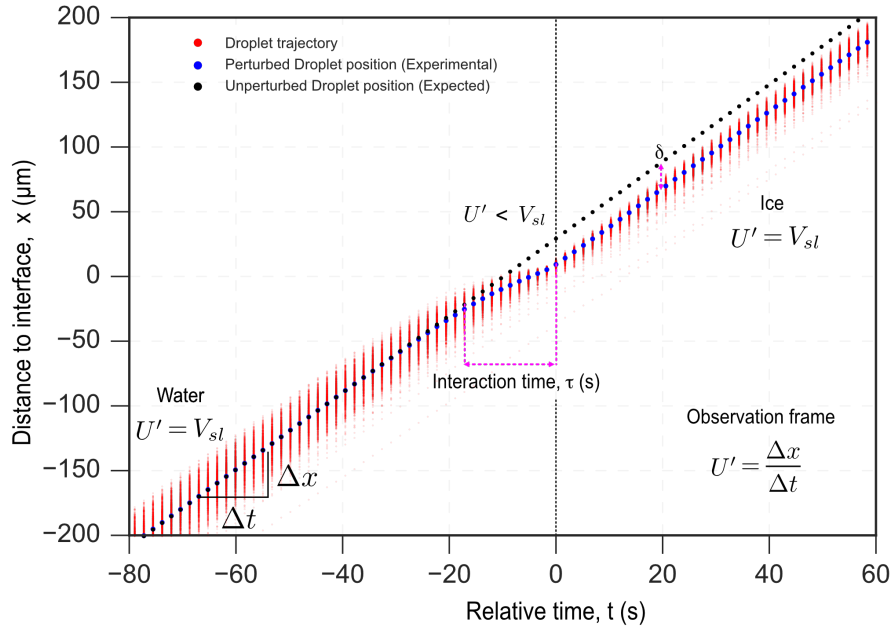


Figure S1: **Measurement of interaction time and apparent droplet velocity U' in the observation frame.** In the observation frame, far from the solid-liquid interface in water the droplet moves at the imposed growth rate $U' = V_{sl}$, as the droplet approaches the interface it gets repelled $U' \neq V_{sl}$, and as the droplet is engulfed in the ice it doesn't get repelled anymore, thereby recovering $U' = V_{sl}$. The interaction time is the total duration over which a droplet gets repelled by the solidification interface. Relative time is zero when the front edge of the droplet hits the solidification front. Experimental conditions for which the curve was recorded: $V_{sl} = 3 \mu\text{m} \cdot \text{s}^{-1}$, $G = \nabla T = 10^4 \text{K} \cdot \text{m}^{-1}$, Droplet size $R_1 = 7.2 \pm 0.4 \mu\text{m}$. © (2020) S. Tyagi *et al.* (10.6084/m9.figshare.14815083) CC BY 4.0 license <https://creativecommons.org/licenses/by/4.0/>.

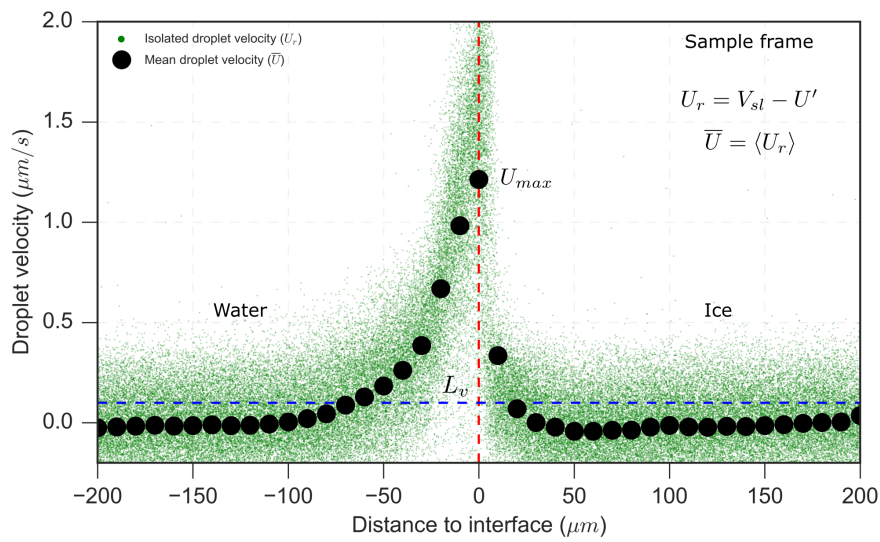


Figure S2: **Deducing the isolated droplet velocity U_r and the mean droplet velocity \bar{U} in the sample frame.** In the sample frame, the isolated droplet velocity U_r is zero far from the interface, it increases and reaches a maximum when the droplet gets repelled by the interface and subsequently, reduces to zero as the droplet is engulfed in the ice. Experimental conditions for which the curve was recorded: $V_{sl} = 3 \mu m \cdot s^{-1}$, $G = \nabla T = 10^4 K \cdot m^{-1}$, Droplet size $R_1 = 7.2 \pm 0.4 \mu m$. © (2020) S. Tyagi *et al.* (10.6084/m9.figshare.14815083) CC BY 4.0 license <https://creativecommons.org/licenses/by/4.0/>.